



Regulating intragap states in colloidal quantum dots for universal photocatalytic hydrogen evolution

Mengke Cai^a, Xin Tong^{a,*}, Hongyang Zhao^a, Peisen Liao^b, Liang Pan^a, Guangqin Li^{b,*}, Zhiming M. Wang^{a,c,**}

^a Institute of Fundamental and Frontier Sciences, University of Electronic Science and Technology of China, Chengdu 610054, PR China

^b School of Chemistry, Sun Yat-Sen University, Guangzhou 510275, PR China

^c Institute for Advanced Study, Chengdu University, Chengdu 610106, PR China

ARTICLE INFO

Keywords:

Colloidal quantum dots
Defect engineering
Hot-electron
Intragap states
Photocatalytic hydrogen generation

ABSTRACT

Understanding and manipulating intragap states in semiconductors may enable superior solar-to-hydrogen energy conversion. The effect of intragap states on photocatalysis usually remains unclear and is sometimes contradictory. Quantum-confined colloidal quantum dots (QDs) provide a unique platform to tune the density and distribution of intragap states due to their discrete energy levels. Herein, intragap active domains, composed of Cu vacancies (V_{Cu}') and high-valent Cu (Cu^*) defect states, are constructed in copper-deficient Zn-doped $CuInS_2$ QDs. Note that these intragap states mainly exist at in-facet and on-edge defects in QDs, being away from the valence band maximum and close to Fermi level. Steady and transient optical spectra indicate that photo-activated Cu^* states serving as photoinduced absorption centers can facilitate the generation of long-lived hot electrons (ca. 85 ps) as a manifestation of phonon bottleneck. Synergistically, the V_{Cu}' states enable the holes capture and electron-hole pairs decoupling to suppress ultrafast Auger-like hot carrier cooling (ca. 178 fs). Moreover, the on-edge defects are demonstrated to play an active role in mediating proton reduction kinetics through density functional calculation. As a result, the QDs exhibit an outstanding hydrogen generation rate of $50.4 \text{ mmol g}^{-1} \text{ h}^{-1}$ without any noble metal, meanwhile, various molecule oxidation and polymer degradation can be integrated with the hydrogen generation process.

1. Introduction

Harvesting solar energy to generate hydrogen represents a promising and sustainable avenue to solve the global energy crisis [1,2]. Efficient solar-to-hydrogen energy conversion relies on suitable semiconductor-based photocatalytic materials [3–5]. Unfortunately, pure phase semiconductor usually maintain a low energy conversion efficiency due to the limited solar absorption, poor charge carrier separation, and weak active sites [6,7]. Thereafter, defect engineering has been developed to tune their photocatalytic performance by manipulating defects such as dopants, vacancies and interstitials [8,9]. The well-known advances include Mo-doped $BiVO_4$ [10,11], Al-doped $SrTiO_3$ [12], and oxygen-vacancy-containing black TiO_2 [13]. Crucially, all of these advances have been enabled by control over the concentration of defects, which can drastically affect the number and energy of intragap states in semiconductors.

Defects create intragap states [14,15], which are responsible for various carrier phenomena detrimental or beneficial to the electronic properties of solar energy conversion materials [14]. For instance, relatively deep intragap states act as Shockley-Read-Hall (SRH) recombination centers that reduce energy conversion efficiency [16]. In contrast, shallow intragap states usually serve as charge trapping centers. Wu et al. discovered the intragap states associated with Cu dopants could participate in hole trapping process, facilitating long-lived hot electron relaxation [17,18]. Photoactive deep/shallow intragap states also enable longer-wavelength optical transitions between intragap states and band states [19–21]. Sub-bandgap transitions stemming from Cu-related intragap states were reported in the works by Kamat et al. [19], and by Klimov et al. [20,21]. However, the current literature mainly emphasize the role of intragap states, neglecting the intrinsic structure-activity relationships between intragap states and defects, especially the distribution and interaction of defects. Thus, precise

* Corresponding authors.

** Corresponding author at: Institute of Fundamental and Frontier Sciences, University of Electronic Science and Technology of China, Chengdu 610054, PR China.

E-mail addresses: xin.tong@uestc.edu.cn (X. Tong), liguangqin@mail.sysu.edu.cn (G. Li), zhmwang@uestc.edu.cn (Z.M. Wang).

control over the concentration, distribution, and interaction of defects, which create abundant intragap states, would be a powerful tool for photocatalytic hydrogen generation.

Colloidal quantum dots (QDs) are quantum-confined semiconductors with discrete energy levels and ultra-high surface-to-volume atomic ratios, which can be tailored by adjusting composition and size [22–27]. Therefore, QDs are promising research objects to control the number and energy of intragap states for optimized activity of photocatalytic hydrogen generation. As typical environment-friendly I-III-VI₂ colloidal QDs, CuInS₂-based QDs photocatalysts have demonstrated substantial potential in solar hydrogen production. However, CuInS₂-based QDs usually suffer from severe interfacial recombination of charge carriers and poor catalytic kinetics due to weak catalytic active sites and deep defect states. To optimize catalytic kinetics, researchers have combined the homogeneous [28] and heterogeneous [29] co-catalysts with QDs to enhance the interfacial electron transfer efficiency. Recently, Shi and co-workers also employed carbon dots as an effective hole transfer intermediate between sacrificial agent and QDs to facilitate the electron extraction [30]. Meanwhile, crystal phase engineering [31], ligand engineering [32], doping [33,34], heterojunction engineering [35], and core-shell construction [36] have been studied, aiming to inhibit the recombination of photo-generated carriers. Additional strategy to suppress interfacial charge recombination is defect engineering by defect passivation, which is also beneficial to the catalytic kinetics using defects. For example, Ning and co-workers concluded that Cu vacancies are the main source of defects in QDs [32], leading to unexpected charge recombination. Another research demonstrated a controlled amount of Cu defects in CuInS₂-based QDs could enhance carrier concentrations/lifetimes of the QDs [37]. Other report was proposed that the Cu vacancies could simultaneously optimize charge carrier dynamics to boost the generation of long-lived active electrons [38], even enhancing hydrogen's adsorption energy with an obvious decrease in transition state energy barrier.

In this work, we introduced Cu vacancies (V_{Cu}') into highly defect-tolerant Zn-doped CuInS₂ colloidal (ZCIS) QDs via a synthetic method. The V_{Cu}' are generated by the following defect reaction Eq. (1) according to the Kröger-Vink notations [39,40]:



The formation of defect pairs consisting of the Zn-substituted Cu site (Zn_{Cu}^{\bullet}) and V_{Cu}' is energetically favorable under Cu-poor condition [40], wherein the Zn dopants enables the formation of stable chalcopyrite QDs. [22,24,41,42] Instead, Zn^{2+} tends to replace Cu^+ and In^{3+} simultaneously under Cu-stoichiometric condition (Cu:In=1:1) [43], according to Eq. (2) as follows:



Hence, simultaneously controlling the zinc-substitution and copper-deficient growth environment can induce the generation of the V_{Cu}' [22, 24,41,42]. Moreover, the V_{Cu}' in QDs can create a void with dangling bonds around the adjacent atoms, causing the local structural relaxation around the localized V_{Cu}' site [14]. Accordingly, the charge delocalizes across neighboring atoms, creating intragap states associated with photoactivated Cu defects (Cu^*) [14,20,21], such as high-valent Cu_{Cu}^{\bullet} species. Because of the large surface-to-volume atomic ratio, these intragap states are mainly located at the surface defects, rather than bulk defects [14].

Femtosecond transient absorption (fs-TA) measurements revealed that V_{Cu}' site could fully capture photogenerated holes and decoupled the photogenerated electron-hole pairs, which further confirmed that photoactivated Cu^* states could generate hot electrons for proton reduction. Detailed density functional theory (DFT) calculations showed that these intragap states were distributed over a wide range, regulating the electronic structure to activate the reactive intermediates. As a result, the V_{Cu} -high ZCIS QDs exhibited superior photocatalytic activity

for hydrogen generation. To further verify the universality, up to 24 types hole sacrificial agents are used to couple hydrogen evolution, including bioactive molecule oxidation and polymer degradation. Besides that, outdoor natural sunlight-driven hydrogen production experiments verify the superior solar-to-hydrogen energy conversion schemes for practicability.

2. Experimental section

2.1. Materials

Copper(I) iodide (CuI), indium(III) acetate ($\text{In}(\text{Ac})_3$), 1-dodecanethiol (DDT), oleylamine (OLA), 3-mercaptopropionic acid (MPA), 1-octadecene (ODE), N,N-dimethylformamide (DMF), zinc acetate dehydrate ($\text{Zn}(\text{Ac})_2 \times 2\text{H}_2\text{O}$), isopropanol, methanol, ethanol, triethanolamine, lactic acid, urea, thiourea, thioacetamide, 1,3-dimethylthiourea, sodium sulfite, mercaptoethanol and toluene were purchased from Sigma-Aldrich. Ascorbic acid (AA), sulfur powder (S), cysteine, penicillamine, histidine, glutathione, glucose, sucrose, dopamine, polyethylene glycol, polylactic acid, cellulose, mercaptopropionic acid and polyethylene terephthalate were purchased from Aladdin. Commercial Adamas-beta® g-C₃N₄ was purchased from Adamas. Evonik AERO-XIDE® P25 TiO₂ was purchased from Evonik Industries AG (Hanau, Germany). All chemicals were used without further purification.

2.2. Synthesis of ZCIS, V_{Cu} -low ZCIS, V_{Cu} -medium ZCIS and V_{Cu} -high ZCIS QDs

QDs were fabricated by a two-step process reported by our previous work with slight modifications [22]. CuI (1 mmol (ZCIS), 0.5 mmol (V_{Cu} -low ZCIS), 0.25 mmol (V_{Cu} -medium ZCIS), 0.125 mmol (V_{Cu} -high ZCIS)), ($\text{Zn}(\text{Ac})_2 \times 2\text{H}_2\text{O}$) (0.5 mmol) and $\text{In}(\text{Ac})_3$ (1 mmol) were mixed with DDT (5 mL) and OLA (5 mL) in a 50 mL flask and degassed under vacuum at 100 °C for 30 min. The temperature was then raised to 140 °C and maintained for 15 min to fully dissolve the precursors. Meanwhile, OLA-S solution (0.5 M) was prepared by mixing S (2 mmol) powder with OLA (4 mL) at room temperature. Subsequently, the reaction mixture was heated to 230 °C for 10 min to conduct QD's nucleation using S-containing DDT as S source. Next, the OLA-S solution (0.5 M) was quickly injected via syringe, and then the flask was cooled quickly down to a growth temperature of 200 °C and maintained for 20 min. The reaction was then quenched with cold water, and ligand exchange was conducted on the QDs afterwards. Typically, the MPA-containing DMF solution was first prepared by mixing 4 mL of MPA and 24 mL of DMF. The stock solution containing as-synthesized QDs (2 mL) was mixed with the MPA-containing DMF solution and degassed under vacuum at 50 °C for 30 min, which was then heated to 120 °C for 15 min to conduct ligand exchange. The reaction was then quenched with cold water, and the stock solution was precipitated with isopropyl alcohol (30 mL) solution, centrifuged to eliminate unreacted precursors, and redispersed in water (30 mL). The QDs-contained aqueous solution are used for photocatalytic H₂ generation.

2.3. Photocatalytic reactions

QDs samples were prepared in a 50 mL screw cap vial equipped with a micro stir bar and closed with silicone/PTFE septum. The QDs-contained aqueous solution (3 mL), H₂O (2 mL) and ascorbic acid (88 mg, 100 mM) were put in the vial. Before the reaction, the system was evacuated by a mechanical pump and then filled with 101 kPa of high-purity N₂. This process was repeated three times to completely remove O₂ from the system and the last time the vial was filled with N₂ gas. Photocatalytic H₂ generation was performed on multichannel photochemical reaction system (PCX-50 C, Beijing Perfectlight Technology Co., Ltd.). A white-light LED lamp ($\lambda = 380\text{--}780\text{ nm}$, light intensity = 100 mW cm⁻²) was used as the solar simulator illumination for

the photocatalytic reaction.

2.4. DFT calculations

We carried out all the DFT calculations in the Vienna ab initio simulation (VASP5.4.4) code [44]. The exchange-correlation is simulated with PBE functional and the ion-electron interactions were described by the PAW method [45,46]. The vdWs interaction was included by using empirical DFT-D3 method [47]. A $15.73 \times 17.31 \times 29.37 \text{ \AA}$ cell ($90^\circ \times 90^\circ \times 90^\circ$) was constructed to accommodate the $\text{CuZnIn}_2\text{S}_4$ models. The Monkhorst-Pack-grid-mesh-based Brillouin zone k-points are set as $2 \times 2 \times 1$ for all periodic structure with the cutoff energy of 450 eV. The convergence criteria are set as 0.01 eV \AA^{-1} and 10^{-5} eV in force and energy, respectively.

The free energy calculation of species adsorption (ΔG) is based on Nørskov et al.'s hydrogen electrode model [48], according to Eq. (3) as follows:

$$\Delta G = \Delta E + \Delta E_{\text{ZPE}} + \Delta H_{0 \rightarrow T} - T\Delta S + eG_U \quad (3)$$

Herein ΔE , ΔE_{ZPE} , and ΔS respectively represent the changes of electronic energy, zero-point energy, and entropy that caused by adsorption of intermediate. The $\Delta H_{0 \rightarrow T}$ refers to the change in enthalpy when heating from 0 K to T K. The entropy of $\text{H}^+ + \text{e}^-$ pair is approximately regarded as half of H_2 entropy in standard condition [49].

2.5. Characterizations

UV-Vis absorption spectra was measured using Shimadzu UV-3101 PC. PL spectra of QDs were measured via FLS 920 fluorescence spectrometer with 460 nm laser excitation. TEM images were obtained by FEI/TECNAI G2 F20 HRTEM system. XRD patterns were recorded using a Bruker D8 ADVANCE A25X with $\text{Cu K}\alpha$ radiation. XPS and UPS measurements were performed by a Thermo Fisher Scientific Escalab 250Xi high vacuum system. The gas products were measured by a GC system (Shimadzu GC-2014). The ICP-OES (Plasma 1000) was used to estimate the concentration of elements in QDs-contained aqueous solution.

2.6. Transient absorption measurement

Measurements were performed by equipping a regeneratively amplified Ti:sapphire laser source (Coherent Legend, 800 nm, 150 fs, 5 mJ per pulse, and 1 kHz repetition rate) and Helios (Ultrafast Systems LLC) spectrometer. A portion of the 800 nm output (75 %) pulse was frequency-doubled in a BaB_2O_4 (BBO) crystal, which could generate a wavelength-tunable laser pulse as pump beam; meanwhile, the remaining portion of the output was concentrated into a sapphire window to produce white light continuum (420–780 nm) probe light. The pump beam was formed from part of the 800 nm output pulse from the amplifier, and its power was adjusted by a range of neutral-density filters. The pump beam was focused at the sample with a beam waist of about $\sim 360 \mu\text{m}$. A mechanical chopper was employed to modulate the pump repetition frequency to 1/2 the probe repetition rate. The probe pulse was recorded using a fiber-optics-coupled multichannel spectrometer, and the optical path in the samples was 5 mm. The samples were vigorously stirred in all the measurements.

2.7. Photoelectrochemical tests

Photoelectrochemical Measurements were evaluated by using an electrochemical workstation (PARSTAT 3000A-DX with 20 mV/s sweep rate) coupled with a class AAA solar simulator (SAN-EI, XES-50S1), wherein the used standard three-electrode system is composed of the as-fabricated QDs-photoelectrodes as working electrode, a Ag/AgCl reference electrode (saturated in 4 M KCl) and a Pt foil counter electrode. For prepared working electrode, the QDs-contained aqueous solution (480 μL) and Nafion (20 μL) were mixed and dispersed by

ultrasonic for 30 min. The working electrodes were obtained through dripping the catalyst ink on the F-doped SnO_2 coated glass (FTO) electrode. 0.1 M AA solution was chosen as electrolyte. Linear sweep voltammetry (LSV) were measured at a scan rate of 5 mV/s. The potential in the LSV polarization curves were corrected for iR compensate. Current density-time ($J-t$) plots were collected at -0.8 V versus Ag/AgCl reference electrode potential under chopped illumination. The EIS plots were collected via the above-mentioned three-electrode system under parameters of 0.1 Hz to 10 kHz with 10 mV amplitude at open circuit voltage.

3. Results and discussion

3.1. Hypothesis setting and intragap states

Notably, while bulk defect states can affect carrier dynamics, intragap states on the surface are able to influence both carrier dynamics and catalytic kinetics [14]. Therefore, we proposed a hypothesis for the surface distribution of intragap states shown in Fig. 1a. The prevailing defects are in-facet due to lower defect formation energy in V_{Cu} -low ZCIS QDs than on-edge defects, which will be discussed in the next section. With increasing copper deficiency, the in-facet and on-edge defect pairs coexist on the surface of V_{Cu} -high ZCIS QDs, which were proved by combining experimental results and theoretical calculations. The unique distribution of intragap states enables superior photocatalytic energy conversion schemes.

From a carrier dynamics viewpoint (Fig. 1b), abundant photo-activated Cu^* states can generate hot electrons due to their higher intragap energy levels (causing photoinduced absorption, PIA) compared to the lower valence band (VB) energy levels (mainly stimulating exciton absorption, XA) under the same excitation conditions, as the energy of hot electrons (red sphere) is above the band edge electrons (black sphere) [50,51]. The relaxation of hot electrons in QDs usually follow two channels: (i) A slow hot electrons cooling through the longitudinal optical (LO) phonons (red arrow), called phonon bottleneck [52]. It is due to that energy levels, especially in CB of QDs, are sparsely spaced with the inter-level energy gap substantially higher than the LO phonon energy [53]. (ii) A ultrafast Auger-like process wherein the hot electrons lose its excessive energy by transferring it to holes (blue arrow) [52,54,55], and the holes rapidly relax via phonon emission due to a large density of states in the VB. In this work, abundant V_{Cu} states can fully capture photogenerated holes [17,18], avoiding the ultrafast hot electron relaxation via the Auger-like cooling process. Therefore, photocatalysis utilizing hot electrons can work via phonon bottleneck and prolonged hot electron lifetime.

From a catalytic kinetics viewpoint (Fig. 1c), intragap states associated with on-edge defects usually suggest weak steric hindrance and low energy barrier [8,9,56,57]. In addition, the intragap states near Fermi level can optimize adsorption strength for the proton reduction intermediates [58–60]. In subsequent experiments and calculations, our hypothesis has been validated.

3.2. Physical and chemical structure characterization

As a control sample, the stoichiometric ZCIS QDs ($\text{Cu:In}=1:1$) were prepared using a published method [22]. In contrast, the V_{Cu} was introduced into QDs to synthesize V_{Cu} -low ZCIS ($\text{Cu:In}=1:2$), V_{Cu} -medium ZCIS ($\text{Cu:In}=1:4$) and V_{Cu} -high ZCIS ($\text{Cu:In}=1:8$) QDs by modulating copper-deficient growth environment. The copper deficiency can be controlled by reducing the content of Cu precursor (CuI) during QDs' synthesis (Details in Experimental Section). Elemental composition analysis, conducted using inductively coupled plasma-optical emission spectroscopy (ICP-OES), displayed Cu-to-In ratios of 1:1.2, 1:1.9, 1:3.9 and 1:6.7 in the ZCIS, V_{Cu} -low ZCIS, V_{Cu} -medium ZCIS and V_{Cu} -high ZCIS QDs (Table S1), respectively. X-ray diffraction (XRD) patterns showed that the crystal phase of these QDs was between chalcopyrite

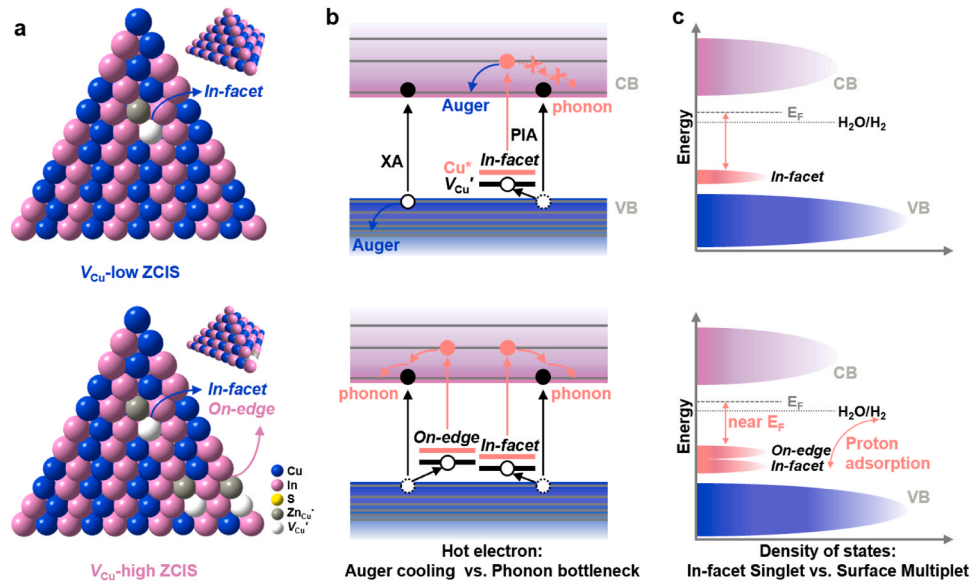


Fig. 1. Schematic diagram of intragap states. (a) Surface defect state types, wherein *in-facet* defects are prevailing under low vacancy concentration condition. (b) Proposed hot electron relaxation mainly including a pair of competitive processes: a slow hot electrons cooling (red arrow) and a ultrafast Auger-like process (blue arrow). (c) Proposed band structure and hypothetical density of states in V_{Cu} -low ZCIS (top) and V_{Cu} -high ZCIS (bottom) QDs.

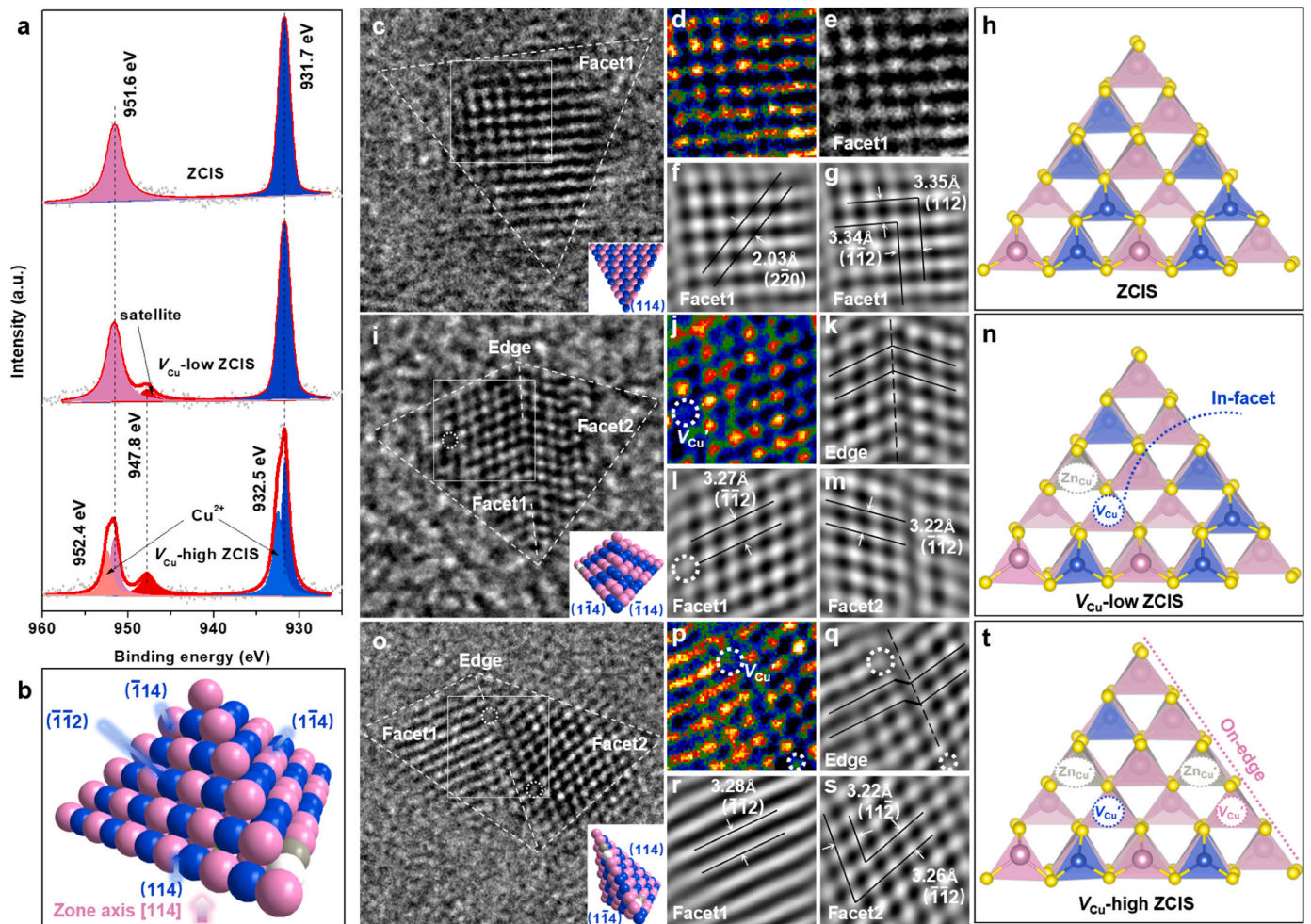


Fig. 2. Structure characterization of QDs. (a) High-resolution XPS Cu 2p spectra of as-prepared QDs. (b) Crystallographic model of the trigonal pyramidal-shaped QDs. (c, i, o) TEM images, (d, j, p) the heat map mode from selected box area in TEM images, (e-g, k-m, q-s) partial magnification images and (h, n, t) schematic diagrams of ZCIS (c-h), V_{Cu} -low ZCIS (i-n) and V_{Cu} -high ZCIS (o-t). Insets in (c), (i) and (o) are crystallographic model with specific orientation.

and zinc blende due to zinc doping (Fig. S1). The targeted incorporation of V_{Cu} defects in ZCIS QDs was detected using electron paramagnetic resonance (EPR) spectra, which showed a strong signal referring Cu defect around $g = 1.995$, indicating that a large amount of single electrons were paired and implying the presence of abundant V_{Cu} in copper-deficient ZCIS QDs (Fig. S2) [61,62]. Moreover, the intensity of EPR signal enhanced with decreasing Cu-to-In ratios, implying the gradual increase of V_{Cu} concentrations (Fig. S3).

X-ray photoelectron spectroscopy (XPS) was also conducted to investigate the electronic states associated with V_{Cu} (Figs. 2a and S4–5). For the Cu 2p spectra of all QDs, the deconvoluted peaks centered at 931.7 eV (Cu 2p_{3/2}) and 951.6 eV (Cu 2p_{1/2}) are assigned to Cu¹⁺, whereas the additional peaks at 932.5 eV and 952.4 eV are ascribed to Cu²⁺ appeared in V_{Cu} -high ZCIS QDs [61,63–65]. More importantly, the Cu satellite peak at 947.8 eV (derived from the Cu²⁺ species) manifest sharp feature for Cu-deficient ZCIS QDs in contrast with nearly no satellite peak signal for ZCIS QDs [66], further proving the existence of Cu²⁺. With increasing copper deficiency, the ratio of high-valent Cu²⁺ species in QDs was varied from none (ZCIS QDs) to approximately 49 % (V_{Cu} -high ZCIS QDs, Table S2). The contents of Cu²⁺ increase in Cu-deficient ZCIS QDs, confirming the formation of V_{Cu} [63,65].

Transmission electron microscopy (TEM) images indicate that these QDs exhibit a typical pyramidal shape with an average diameter of 3.2–3.3 nm (Fig. S6) [41]. According to the size statistics and

crystallographic orientations [67], we construct a crystallographic structure model composed of six-layer metal atoms stacked together (Fig. 2b, the model details can be found in Fig. S7). Due to fast growth in the [11–2] direction, chalcopyrite QDs usually form a relatively stable (–1 to 12) surface facet [67]. For example, the QDs in Fig. 2b is on (114) surface facets viewed up the [114] zone axis with exposed (–1 to 12) surface facet. As displayed in Fig. 2c–g, the d_{2-20} , d_{1-12} and d_{11-2} spacings are measured to be 0.203, 0.334 and 0.335 nm on the (114) surface facet, testifying the [114] orientation of as-synthesized ZCIS QDs. As for V_{Cu} -low ZCIS QDs (Fig. 2i–m), the (1–14) surface facet shows obscure lattice image in dotted circle, implying the existence of V_{Cu} [61,63,68]. Such remarkable lattice defects exist more in V_{Cu} -high ZCIS QDs (Fig. 2o–s), especially on the edge sites. As shown in Fig. 2q, the amplified images disclose edge areas of dislocation between (1–14) and (114) surface facet for V_{Cu} -high ZCIS QDs, in contrast with the neat edge in Fig. 2k for V_{Cu} -low ZCIS QDs. The results demonstrate the tunable concentration and distribution of V_{Cu} defects in QDs. Theoretical simulations were performed to support our experimental observations. Defect calculations indicate that introducing in-facet defects is more compatible than on-edge defects in V_{Cu} -low ZCIS QDs (Fig. S8–9), due to the lower defect formation energy of in-facet defects. Thus, three ideal distribution models of defect states are concluded in Fig. 2h, n and t, respectively for ZCIS, V_{Cu} -low ZCIS and V_{Cu} -high ZCIS QDs, which is consistent with the experimental results.

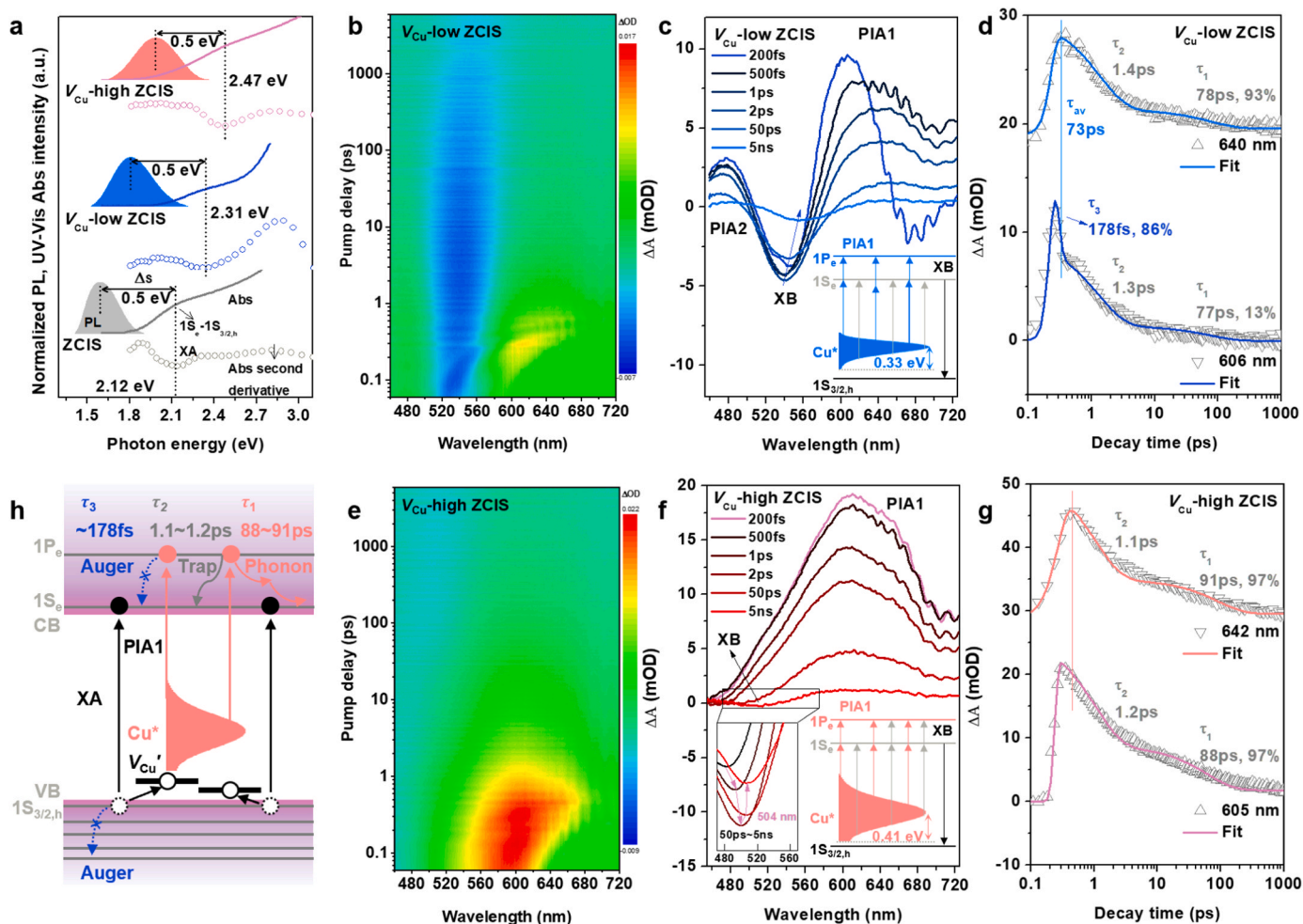


Fig. 3. Spectral analysis of carrier dynamics. (a) PL emission (colored shading), UV-vis absorption (solid line) and its second derivative spectra (dotted line) of QDs. (b, e) 3D contour plots of fs-TA spectra. The fs-TA spectra and kinetic traces of (c, d) V_{Cu} -low ZCIS and (f, g) V_{Cu} -high ZCIS QDs. (h) Schematic of carrier dynamics involved in V_{Cu} -high ZCIS QDs. In a typical V_{Cu} -high ZCIS QD, there is more probability that broadly distributed Cu²⁺ states induce generation of hot electrons via PIA1 process. Ultrafast hole capturing by abundant V_{Cu} states decouple electrons and holes, thus blocking Auger-like relaxation process and enabling a phonon bottleneck for long-lived hot electrons.

3.3. Steady and transient optical characterization

To understand the effect of intragap states on carrier dynamics, ultraviolet-visible (UV-vis) absorption, photoluminescence (PL) emission and fs-TA measurements were performed and shown in Fig. 3. By taking a second derivative of the UV-vis absorption spectra, we obtain the lowest exciton absorption (XA, 2.1–2.5 eV), attributed to the transition from the first hole quantized state $1S_{3/2,h}$ to the first electron quantized state $1S_e$ in QDs [18,41,69]. A large Stokes shift (Δ_s , 400–500 meV) is observed between PL emission and XA peak for all QDs (Fig. 3a and Fig. S10), wherein the Cu^* intragap states are responsible for such large Δ_s , due to intragap emission from delocalized conduction band (CB) to localized Cu^* intragap states [20,21]. Besides, we also observed a strong PL broadening (Fig. 3a and Table S3), which showed a calculated FWHM of ~260, 330, 360 and 410 meV for ZCIS, V_{Cu} -low ZCIS, V_{Cu} -medium ZCIS and V_{Cu} -high ZCIS QDs, indicating a remarkable broadening in the heterogeneity of the Cu^* defects [70].

Pump-probe fs-TA tests provided more dynamic details of Cu^* intragap states. The pump pulse was tuned at 3.2 eV (excited at 387 nm) with a low pump fluence of $14 \mu J cm^{-2}$ under single-exciton-dominated conditions, wherein average exciton number per QD, $\langle N \rangle \sim 0.12$, was estimated suppressing multiple exciton effects (see Fig. S11 and notes for details) [17,18]. The QDs were vigorously stirred during all the measurements in order to minimize photocharging effects [71,72]. The probe pulse was a broad-band white light continuum (time decay from 60 fs to 6 ns). We investigated ultrafast carrier dynamics in V_{Cu} -low ZCIS QDs as a benchmark. Fig. 3b shows the 3D fs-TA counter plot, in which a long-lived exciton bleach (XB) and two short-lived PIA signals are observed (Fig. 3c). The XB features of $1S_e$ - $1S_{3/2,h}$ exciton arise from the state-filling effect of the $1S_e$ electron at ~540 nm [51,73], consistent with the wavelength of the steady-state XA peak. A red shift of the bleach maximum wavelength takes place, which could be attributed to the dynamics of hole trapping by the V_{Cu}' [74,75]. Similarly, the V_{Cu} -medium ZCIS QDs show consistent characteristics with V_{Cu} -low ZCIS QDs in the fs-TA spectra (Fig. S12), i.e., a long-lived XB and two PIA signals. The main decay time constant (τ_1) of XB band (amplitude coefficients > 90 %) delayed by up to 1.7 ns for both V_{Cu} -low ZCIS and V_{Cu} -medium ZCIS QDs (Fig. S13), which originates from either radiative or non-radiative $1S_e$ - $1S_{3/2,h}$ exciton recombination showing similar decay dynamics [76]. On the contrast, the fast decay time constant (τ_2) is most likely due to trapping at V_{Cu}' associated with dangling bonds [76]. As there is a higher V_{Cu}' density in V_{Cu} -medium ZCIS QDs, the τ_2 of fast decay (23 ps) is shorter than that (71 ps) of V_{Cu} -low ZCIS QDs.

The derivative-like features from 465 to 490 nm (PIA2) reflect the Stark-like effect features of higher-energy exciton (such as $1P_e$ - $1P_{3/2,h}$) deriving from its Coulomb interaction with lower-energy $1S_e$ - $1S_{3/2,h}$ exciton [17,18,77]. On contrast, a broad positive absorption (PIA1) band on the red side of the XB signal is observed. We attribute the broad band to the electron transitions localized on the photoactivated Cu^* intragap states where the electron is excited to a CB level ($1S_e$ or $1P_e$). The Cu^* states become optically active after some photon event activates them, presumably via hole trapping into neighboring V_{Cu}' states [21]. If so, this transition will be expected to strongly depend on the position and distribution of the Cu^* intragap states. Due to the broad heterogeneity of Cu^* intragap states, the deep intragap states far from VB (blue arrow) enable both the transition of $Cu^* - 1P_e$ and $Cu^* - 1S_e$, whereas the shallow intragap states near VB (gray arrow) only involve the transition of $Cu^* - 1S_e$ restricted by the low-energy photon absorption (Insets in Fig. 3c). This explains why the PIA1 band is unusually asymmetric with narrow high-energy blue side and wide low-energy red side. Furthermore, kinetics fitting was conducted to distinguish these two types of intragap transitions (Fig. 3d and Table S4). The low energy red side have a delay in the decay of the PIA1 compared to high energy blue side, that is associated with the capture of the holes from the VB into V_{Cu}' states. This is likely due to that shallow V_{Cu}' states near VB have a greater ability to capture holes so that low energy red side delays the

decay process. The low-energy red side (640 nm) show a bi-exponential recover features: (i) The long delay up to 78 ps (τ_1 , 93 %) refers to the slow electron cooling in QDs [78], because the electron relaxation coupled with longitudinal-optical phonons are inefficient in strong quantum-confined QDs, which is called a phonon bottleneck [17,79]. (ii) The following decay ($\tau_2 = 1.4$ ps, 7 %) is traced to the electron trapping in shallow trap states in or near CB [15,41,78]. On the contrary, the sub-ps decay ($\tau_3 = 178$ fs, 86 %) is identified in the high-energy blue side (606 nm). The ultrafast relaxation of the $1P_e$ hot electron is usually ascribed to an Auger-like process through electron-to-hole energy transfer (Fig. 1b) [17,18]. A similar sub-ps decay ($\tau_3 = 170$ fs, 26 %) can also be observed in the V_{Cu} -medium ZCIS QDs (Fig. S12), yet its amplitude coefficient is much lower than 86 % of V_{Cu} -low ZCIS QDs (Table S4). Meantime, the amplitude coefficient of τ_1 , reflecting electron cooling, has increased from 13 % (V_{Cu} -low ZCIS QDs) to 65 % (V_{Cu} -medium ZCIS QDs). This is likely due to the higher V_{Cu}' concentration in V_{Cu} -medium ZCIS QDs, wherein more holes are captured by V_{Cu}' intragap states. Thereafter, such holes trapping could suppress the sub-ps Auger-like process, and hence promote slow hot electron cooling [17, 18].

We then turned back and focused on the V_{Cu} -high ZCIS QDs, in which both density and heterogeneity of the Cu^* intragap states are more abundant. Fig. 3e-f show an ultra-wide band (PIA1) throughout the entire probe window. Even the PIA1 signal covers the XB band centered at 504 nm, proving that the Cu^* intragap states are abundant in QDs and widely distributed in bandgap. As we proposed, abundant Cu^* intragap states are accompanied with plentiful V_{Cu}' intragap states due to local structural relaxation and charge compensation [14,15]. Because of the synergistic interaction between the Cu^* and V_{Cu}' intragap states, the entire PIA1 features are long-lived (Fig. 3g). Sub-ps decay component can hardly be observed in the high-energy blue side (605 nm). Moreover, the amplitude coefficient of τ_1 for V_{Cu} -high ZCIS QDs reach the maximum proportion of 97 % among three Cu-deficient QDs (Table S4). To summarize, Fig. 3h visually illustrates the entire carrier dynamics in V_{Cu} -high ZCIS QDs: (i) The lowest XA ($1S_e$ - $1S_{3/2,h}$) introduces holes and electrons in VB and CB, respectively. (ii) The V_{Cu}' intragap states can quickly capture holes [17,18,20,21]. After photoactivated via hole trapping into neighboring V_{Cu}' states, the deep Cu^* intragap states enable the transition of $Cu^* - 1P_e$ after absorbing high-energy photons, thus hot electrons are generated on the high-energy blue side of PIA1. (iii) The dynamics of hot electrons is mainly affected by sub-ps Auger-like process and slow electron cooling [17,18,52,55]. Holes capturing process suppresses the Auger cooling of $1P_e$ electrons (blue dotted arrow), and hence long-lived hot electrons can be expected for V_{Cu} -high ZCIS QDs.

3.4. Theoretical simulation

To further support experimental observation, we performed DFT calculation studies for intragap states in our QDs system. In the projected density of states (DOS) profile for ZCIS QDs (Figs. 4a and S14), the dominant feature is Cu 3d orbital in the VB maximum (VBM). The introduction of V_{Cu}' into ZCIS QDs lattice create defect states adjacent to the CB maximum (CBM, medium and upper panel of Fig. 4a) [80]. Notably, the intragap states of the V_{Cu} -high ZCIS QDs were considerably closer to the Fermi level in contrast with V_{Cu} -low ZCIS QDs, suggesting additional charge-transfer channels to enhance the charge mobility and inhibit the recombination of electron-hole pairs [13,80]. Additionally, electrochemical impedance spectroscopy (EIS) presents that the diameter of the Nyquist circle of the V_{Cu} -high ZCIS is much smaller than that of other QDs (Fig. S14). Fitting results indicated that the charge transfer resistance (R_{ct}) was 9, 28 and $44 \Omega cm^{-2}$ for FTO electrodes covered with V_{Cu} -high ZCIS, V_{Cu} -low ZCIS and ZCIS QDs, respectively (Table S5). This proved that the V_{Cu} -high ZCIS QDs possess superior electron conductivity and mobility [81,82], which confirms the DFT simulation results. This may be attributed to the higher electropositivity of on-edge

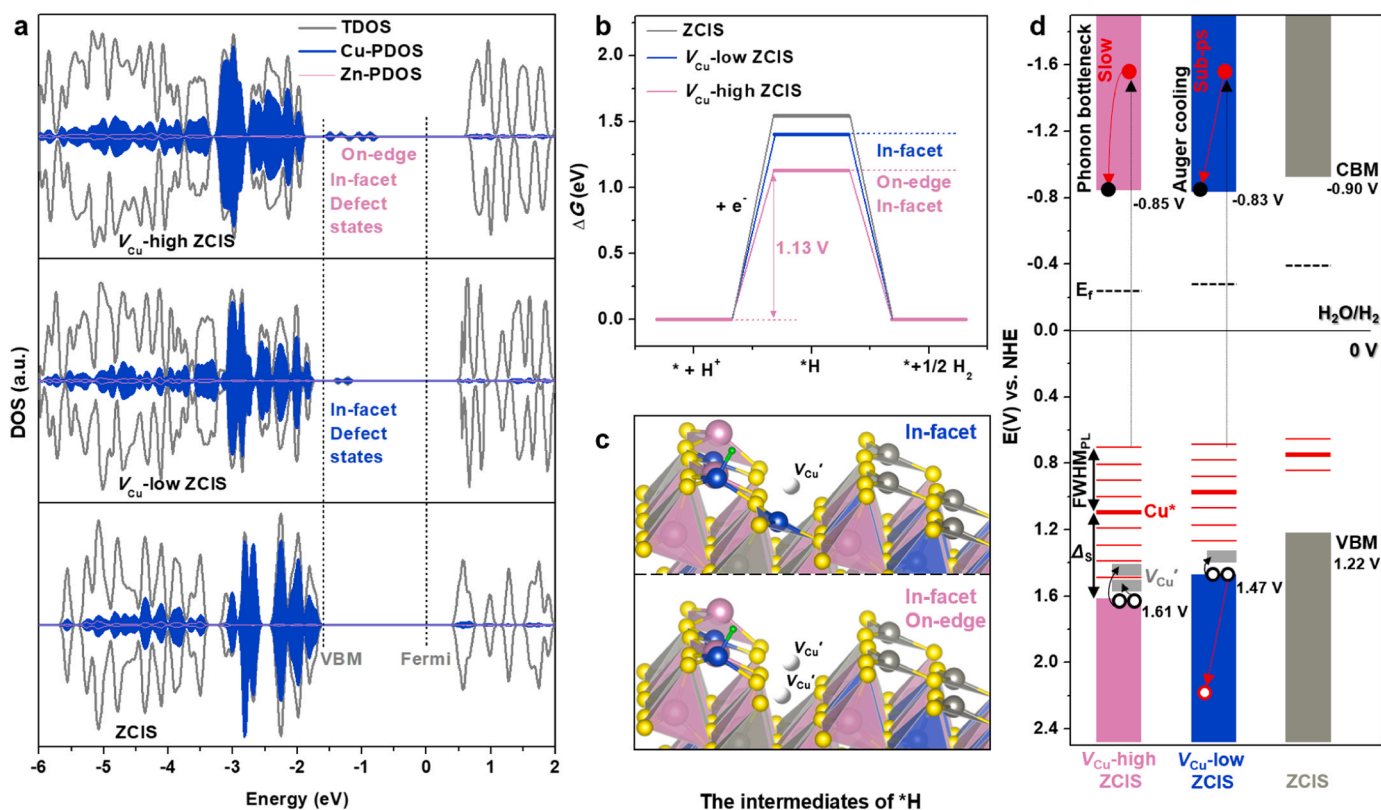


Fig. 4. DFT calculation and band structure for as-prepared QDs. (a) The projected DOS, (b) calculated free energy of the proton reduction reactions, (c) key reaction configurations and (d) Schematic diagram of band structure for ZCIS, V_{Cu} -low ZCIS and V_{Cu} -high ZCIS QDs. The white, blue, gray, pink, yellow and green spheres represent V_{Cu} , Cu, Zn, In, S and H atoms.

Cu^* states than those of in-facet Cu^* states [83], favouring the formation of higher valence Cu^{2+} instead of Cu^{1+} due to stronger local structural relaxation on the edge [14]. It is also consistent with the XPS results in Fig. 2a and Fig. S4, wherein the ratio of high-valent Cu^{2+} is increased with the introduction of V_{Cu} .

Moreover, the local environment of different intragap states can affect the catalytic kinetics for the hydrogen generation. Consequently, we conducted the Gibbs free energy (ΔG) to examine the hydrogen generation activity (Fig. 4b). The proton-assisted electron transfer process requires overcoming a huge activation energy barrier from H^+ to H^* [84–86], where the asterisks denote active sites. Given that on-edge site is more active than in-facet site for proton reduction, [5] the Cu atom on edge was set as catalytic site (Figs. 4c and S15). Note that the ΔG_{H^*} (1.13 eV) of V_{Cu} -high ZCIS QDs is lower than that of other QDs, resulting in the easier bridged spillover of H^* to form hydrogen [61, 87–89]. The band structure of as-prepared QDs was estimated by using UV photoelectron spectroscopy (UPS), wherein the favorable CBM positions are negative to the H_2O/H_2 reduction potential (0 V vs. normal hydrogen electrode, NHE), thus enabling a thermodynamically feasible photocatalytic water reduction reaction (Fig. 4d) [90–92]. More importantly, the band structure based on experimental results is consistent with DFT calculations.

3.5. Photocatalytic activity H_2 evaluation

Given the excellent carrier dynamics and catalytic kinetics of the V_{Cu} -high ZCIS QDs, the photocatalytic hydrogen evolution experiments were then performed under solar simulator irradiation ($380 < \lambda < 780$ nm, 100 mW cm^{-2}) in an aqueous solution with 100 mM ascorbic acid (AA) as the sacrificial agent. According to the Fig. 5a, the V_{Cu} -high ZCIS QDs exhibited excellent hydrogen production activity in the initial reaction time with a subsequently gradual reaction decrease. The photocatalytic

yield reaches up to above 1325 mmol g^{-1} after light irradiation for 24 h, which is almost 95-fold and 265-fold higher than those of V_{Cu} -low ZCIS (14 mmol g^{-1}) and ZCIS (5 mmol g^{-1}) QDs, respectively. Control experiments show that both light and QDs are indispensable for hydrogen evolution (Table S6). Photoelectrochemical characterizations using current-time (J - t) and current-potential (J - V) tests (Figs. 5b and S16) show that the FTO electrodes covered with V_{Cu} -high ZCIS QDs exhibited the strongest photocurrent response ($146 \mu\text{A cm}^{-2}$), which was about 2 and 7 times as higher as that of the ZCIS ($71 \mu\text{A cm}^{-2}$) and V_{Cu} -low ZCIS ($22 \mu\text{A cm}^{-2}$) QDs, respectively. The results also suggest that the V_{Cu} -high ZCIS QDs have the superior ability of light-driven hydrogen generation [84,93,94]. The long-term photocatalytic tests of V_{Cu} -high ZCIS QDs exhibit a considerable photocatalytic durability without the addition of any cocatalyst (such as Pt, IrO_2), as proved by the continuous hydrogen production up to 24 h (Fig. 5c). In addition, the optimal concentration of AA in the system was studied (Fig. S17). Note that nearly 50 % of AA was transformed to dehydroascorbic acid in 100 mM sacrificial agent solution, suggesting that the concentration of AA affects hydrogen production rate and continuously adding ascorbic acid is necessary for long-term reaction. Further long-term reaction was conducted under constant illumination (Fig. S18), refreshing 100 mM AA sacrificial agents every 24 h. The process can continue up to 72 h with a gradual decrease in hydrogen production, which may be due to the deactivation of QDs under long-term illumination. To confirm that electrons were supplied by the AA during long-term reaction, additional quenching tests were performed on the V_{Cu} -high ZCIS QDs. As shown in Fig. S19a, the transient PL decay of QDs became faster after the introduction of more AA. Fitting results reveal that the average lifetime of QDs dropped from 43.9 ns to 29.8 ns with AA concentrations of 500 mM (Table S7), corresponding to a calculated hole transfer rate ($2.3 \times 10^4 \text{ s}^{-1} \text{ mM}^{-1}$) from QDs to AA (Fig. S19b).

Moreover, we summarized the recent reported state-of-the-art

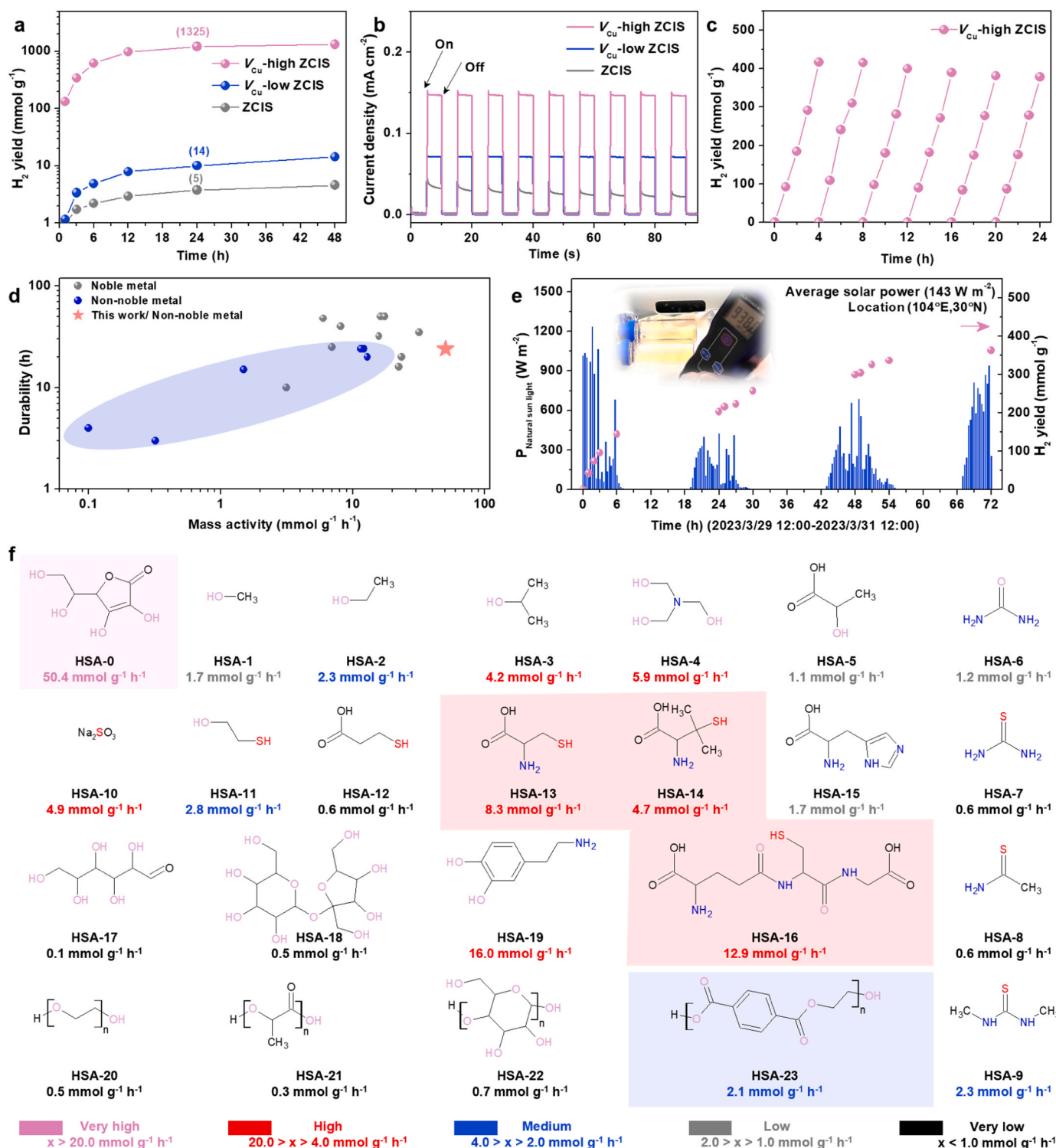


Fig. 5. The photocatalytic hydrogen production performance. (a) Hydrogen yield of the prepared QDs during 48 h solar simulator illumination (380 < λ < 780 nm, 100 mW cm⁻²). (b) Transient photocurrent response. (c) Cycle test of hydrogen yield for V_{cu}-high ZCIS QDs. (d) Efficiency and durability benchmarks of the previously reported photocatalysts for photocatalytic hydrogen production. The statistical performance parameters are shown in Table S8. (e) Natural sunlight-driven hydrogen production of V_{cu}-high ZCIS QDs in 3 days and nights. (f) Universality of hydrogen production coupled with varied hole sacrificial agent oxidation.

photocatalytic hydrogen production systems (Fig. 5d and Table S9) [2–4, 95–97]. Note that the mass activity (50.4 mmol g⁻¹ h⁻¹) and durability (24 h) of hydrogen evolution is achieved by using the noble-free V_{cu}-high ZCIS QDs in this work, which is comparable to those of state-of-the-art noble photocatalysts [98]. Additionally, two standard catalysts, commercial Adamas-beta® g-C3N4 and Evonik AEROXIDE®

P25 TiO₂, were applied in the photocatalytic hydrogen production system under the exact same experimental conditions. The mass activity of 0.35 mmol g⁻¹ h⁻¹ and 0.13 mmol g⁻¹ h⁻¹ was obtained for g-C3N4 and P25 TiO₂ (Tables S6 and S9), respectively, further implying the superior performance of our V_{cu}-high ZCIS QDs (50.4 mmol g⁻¹ h⁻¹) when compared to the two standard catalysts. Moreover, outdoor

sunlight-driven hydrogen generation experiments were performed. As shown in Fig. 5e, stable and continuous hydrogen generation was realized in three days and nights with a variable real-time sunlight power density ($0\text{--}1233\text{ W m}^{-2}$), implying the efficient utilization of natural sunlight for solar fuel production [99,100]. To further generalize this excellent QDs system as a photocatalytic platform, the V_{Cu} -high ZCIS QDs was evaluated in the hydrogen production experiments coupled with a wide range of hole sacrificial agents (HSA) oxidation, as shown in Figs. 5f and S20. For most of the molecule oxidation and polymer degradation reactions, the QDs has good universality toward hole-mediated catalytic oxidation (Table S8). Specifically, the oxidation of HSA containing both amino and thiol groups showed excellent activity, such as cysteine (HAS-13), penicillamine (HAS-14) and glutathione (HAS-16), suggesting a promising potential to detect these key bioactive molecules. In addition, the degradation of polyethylene terephthalate (HAS-23) by using our QDs is desirable and will be further explored in future work.

4. Conclusions

In this work, defect-engineered ZCIS colloidal QDs were used as the versatile platform to tune the intrinsic structure-activity relationships between intragap states and defect states. Through manipulating the interaction and distribution of Cu-related defect states (i.e., V_{Cu} and Cu^*), intragap states-mediating carrier dynamics and catalytic kinetics were fully optimized. The fs-TA spectra revealed that the defect-defect interactions between V_{Cu} and Cu^* could decouple electron-hole pairs and suppress the ultrafast Auger-like hot electron cooling, thus facilitating slow hot electron relaxation and favoring long-lived charge separation. The results of TEM analysis, structural simulation and DFT calculation prove the conceptual discovery of distribution-broadened intragap states from in-facet to on-edge defects, which modulate the electronic structure to activate the reactive intermediates. As a result, the developed V_{Cu} -high ZCIS QDs exhibited an excellent hydrogen generation rate of $50.4\text{ mmol g}^{-1}\text{ h}^{-1}$ even without any cocatalysts. Moreover, the hydrogen production system is universal to couple with various molecule oxidation and polymer degradation. Our work open avenues for designing high-performance photocatalyst platforms, especially controlling intragap states by manipulating defect distribution and interaction.

CRedit authorship contribution statement

Liao Peisen: Data curation, Formal analysis. **Zhao Hongyang:** Formal analysis. **Tong Xin:** Conceptualization, Funding acquisition, Supervision, Writing – review & editing. **Cai Mengke:** Conceptualization, Data curation, Formal analysis, Methodology, Validation, Visualization, Writing – original draft, Writing – review & editing. **Wang Zhiming M.:** Formal analysis, Funding acquisition, Writing – review & editing. **Li Guangqin:** Formal analysis, Funding acquisition, Writing – review & editing. **Pan Liang:** Writing – review & editing.

Declaration of Competing Interest

The authors declare that they have no known competing financial interests or personal relationships that could have appeared to influence the work reported in this paper.

Data availability

Data will be made available on request.

Acknowledgements

X.T. acknowledges the support from National Key Research and Development Program of China (No. 2019YFE0121600), National

Natural Science Foundation of China (No. 22105031, 62011530131) and Sichuan Science and Technology Program (No. 2021YFH0054). Z. M.W. is grateful to the National Key Research and Development Program of China (No. 2019YFB2203400) and the “111 Project” (No. B20030). The authors would like to thank Zhang San from Shiyanjia Lab (www.shiyanjia.com) for the DFT analysis. The first author M.C. would like to thank his wife Jiayuan Yang for unwavering support in his Ph.D.

Appendix A. Supporting information

Supplementary data associated with this article can be found in the online version at doi:10.1016/j.apcatb.2023.123572.

References

- [1] P. Zhou, I.A. Navid, Y. Ma, Y. Xiao, P. Wang, Z. Ye, B. Zhou, K. Sun, Z. Mi, Solar-to-hydrogen efficiency of more than 9% in photocatalytic water splitting, *Nature* 613 (2023) 66–70.
- [2] H. Yang, C. Li, T. Liu, T. Fellowes, S.Y. Chong, L. Catalano, M. Bahri, W. Zhang, Y. Xu, L. Liu, W. Zhao, A.M. Gardner, R. Clowes, N.D. Browning, X. Li, A. J. Cowan, A.I. Cooper, Packing-induced selectivity switching in molecular nanoparticle photocatalysts for hydrogen and hydrogen peroxide production, *Nat. Nanotechnol.* 18 (2023) 307–315.
- [3] Y. Zhang, Y. Li, X. Xin, Y. Wang, P. Guo, R. Wang, B. Wang, W. Huang, A. J. Sobrido, X. Li, Internal quantum efficiency higher than 100% achieved by combining doping and quantum effects for photocatalytic overall water splitting, *Nat. Energy* 8 (2023) 504–514.
- [4] X. Ruan, C. Huang, H. Cheng, Z. Zhang, Y. Cui, Z. Li, T. Xie, K. Ba, H. Zhang, L. Zhang, X. Zhao, J. Leng, S. Jin, W. Zhang, W. Zheng, S.K. Ravi, Z. Jiang, X. Cui, J. Yu, A twin S-scheme artificial photosynthetic system with self-assembled heterojunctions yields superior photocatalytic hydrogen evolution rate, *Adv. Mater.* 35 (2023), 2209141.
- [5] J. Ran, L. Chen, D. Wang, A. Talebian-Kiakalaieh, Y. Jiao, M. Adel Hamza, Y. Qu, L. Jing, K. Davey, S.Z. Qiao, Atomic-level regulated 2D ReSe_2 : a universal platform boost photocatalysis, *Adv. Mater.* 35 (2023), 2210164.
- [6] R. Chen, Z. Ren, Y. Liang, G. Zhang, T. Dittrich, R. Liu, Y. Liu, Y. Zhao, S. Pang, H. An, C. Ni, P. Zhou, K. Han, F. Fan, C. Li, Spatiotemporal imaging of charge transfer in photocatalyst particles, *Nature* 610 (2022) 296–301.
- [7] R. Chen, S. Pang, H. An, T. Dittrich, F. Fan, C. Li, Giant defect-induced effects on nanoscale charge separation in semiconductor photocatalysts, *Nano Lett.* 19 (2019) 426–432.
- [8] J. Xiong, J. Di, J. Xia, W. Zhu, H. Li, Surface defect engineering in 2D nanomaterials for photocatalysis, *Adv. Funct. Mater.* 28 (2018), 1801983.
- [9] A. Kumar, V. Krishnan, Vacancy engineering in semiconductor photocatalysts: implications in hydrogen evolution and nitrogen fixation applications, *Adv. Funct. Mater.* 31 (2021), 2009807.
- [10] K.H. Ye, H. Li, D. Huang, S. Xiao, W. Qiu, M. Li, Y. Hu, W. Mai, H. Ji, S. Yang, Enhancing photoelectrochemical water splitting by combining work function tuning and heterojunction engineering, *Nat. Commun.* 10 (2019) 3687.
- [11] Q. Wang, J. Warnan, S. Rodríguez-Jiménez, J.J. Leung, S. Kalathil, V. Andrei, K. Domen, E. Reisner, Molecularly engineered photocatalyst sheet for scalable solar formate production from carbon dioxide and water, *Nat. Energy* 5 (2020) 703–710.
- [12] T. Takata, J. Jiang, Y. Sakata, M. Nakabayashi, N. Shibata, V. Nandal, K. Seki, T. Hisatomi, K. Domen, Photocatalytic water splitting with a quantum efficiency of almost unity, *Nature* 581 (2020) 411–414.
- [13] X. Chen, L. Liu, F. Huang, Black titanium dioxide (TiO_2) nanomaterials, *Chem. Soc. Rev.* 44 (2015) 1861–1885.
- [14] E. Pastor, M. Sachs, S. Selim, J.R. Durrant, A.A. Bakulin, A. Walsh, Electronic defects in metal oxide photocatalysts, *Nat. Rev. Mater.* 7 (2022) 503–521.
- [15] J.S. Park, S. Kim, Z. Xie, A. Walsh, Point defect engineering in thin-film solar cells, *Nat. Rev. Mater.* 3 (2018) 194–210.
- [16] M. Righetto, S.S. Lim, D. Giovanni, J.W.M. Lim, Q. Zhang, S. Ramesh, Y.K.E. Tay, T.C. Sum, Hot carriers perspective on the nature of traps in perovskites, *Nat. Commun.* 11 (2020) 2712.
- [17] L. Wang, Z. Chen, G. Liang, Y. Li, R. Lai, T. Ding, K. Wu, Observation of a phonon bottleneck in copper-doped colloidal quantum dots, *Nat. Commun.* 10 (2019) 4532.
- [18] J. Wang, L. Wang, S. Yu, T. Ding, D. Xiang, K. Wu, Spin blockade and phonon bottleneck for hot electron relaxation observed in n-doped colloidal quantum dots, *Nat. Commun.* 12 (2021) 550.
- [19] D.H. Jara, K.G. Stamplecoskie, P.V. Kamat, Two distinct transitions in Cu_xInS_2 quantum dots. Bandgap versus sub-bandgap excitations in copper-deficient structures, *J. Phys. Chem. Lett.* 7 (2016) 1452–1459.
- [20] A.S. Fuhr, H.J. Yun, N.S. Makarov, H. Li, H. McDaniel, V.I. Klimov, Light emission mechanisms in CuInS_2 quantum dots evaluated by spectral electrochemistry, *ACS Photonics* 4 (2017) 2425–2435.
- [21] A. Fuhr, H.J. Yun, S.A. Crooker, V.I. Klimov, Spectroscopic and magneto-optical signatures of Cu^{1+} and Cu^{2+} defects in copper indium sulfide quantum dots, *ACS Nano* 14 (2020) 2212–2223.

- [22] M. Cai, X. Tong, H. Zhao, X. Li, Y. You, R. Wang, L. Xia, N. Zhou, L. Wang, Z. M. Wang, Ligand-engineered quantum dots decorated heterojunction photoelectrodes for self-biased solar water splitting, *Small* 18 (2022), 2204495.
- [23] X. Li, X. Tong, S. Yue, C. Liu, A.I. Channa, Y. You, R. Wang, Z. Long, Z. Zhang, Z. Zhao, X.-F. Liu, Z.M. Wang, Rational design of colloidal AgGaS₂/CdSeS core/shell quantum dots for solar energy conversion and light detection, *Nano Energy* 89 (2021), 106392.
- [24] Y. You, X. Tong, A. Imran Channa, H. Zhi, M. Cai, H. Zhao, L. Xia, G. Liu, H. Zhao, Z. Wang, High-efficiency luminescent solar concentrators based on composition-tunable eco-friendly Core/shell quantum dots, *Chem. Eng. J.* 452 (2023), 139490.
- [25] N. Zhou, H. Zhao, X. Li, P. Li, Y. You, M. Cai, L. Xia, H. Zhi, A.I. Channa, Z. M. Wang, X. Tong, Activating earth-abundant element-based colloidal copper chalcogenide quantum dots for photodetector and optoelectronic synapse applications, *ACS Mater. Lett.* 5 (2023) 1209–1218.
- [26] M. Cai, X. Li, H. Zhao, C. Liu, Y. You, F. Lin, X. Tong, Z.M. Wang, Decoration of BiVO₄ photoanodes with near-infrared quantum dots for boosted photoelectrochemical water oxidation, *ACS Appl. Mater. Interfaces* 13 (2021) 50046–50056.
- [27] S.-C. Zhu, Z.-C. Wang, B. Tang, H. Liang, B.-J. Liu, S. Li, Z. Chen, N.-C. Cheng, F.-X. Xiao, Progressively stimulating carrier motion over transient metal chalcogenide quantum dots towards solar-to-hydrogen conversion, *J. Mater. Chem. A* 10 (2022) 11926–11937.
- [28] M. Sandroni, R. Guert, K.D. Wegner, P. Reiss, J. Fortage, D. Aldakov, M. N. Collomb, Cadmium-free CuInS₂/ZnS quantum dots as efficient and robust photosensitizers in combination with a molecular catalyst for visible light-driven H₂ production in water, *Energy Environ. Sci.* 11 (2018) 1752–1761.
- [29] C. Ye, M.D. Regulacio, S.H. Lim, S. Li, Q.-H. Xu, M.-Y. Han, Alloyed ZnS–CuInS₂ semiconductor nanorods and their nanoscale heterostructures for visible-light-driven photocatalytic hydrogen generation, *Chem. Eur. J.* 21 (2015) 9514–9519.
- [30] F. Li, Y. Liu, B. Mao, L. Li, H. Huang, D. Zhang, W. Dong, Z. Kang, W. Shi, Carbon-dots-mediated highly efficient hole transfer in I–III–VI quantum dots for photocatalytic hydrogen production, *Appl. Catal. B* 292 (2021), 120154.
- [31] H. Li, W. Li, W. Li, M. Chen, R. Snyder, C. Bittencourt, Z. Yuan, Engineering crystal phase of polytypic CuInS₂ nanosheets for enhanced photocatalytic and photoelectrochemical performance, *Nano Res.* 13 (2020) 583–590.
- [32] X.-Y. Liu, G. Zhang, H. Chen, H. Li, J. Jiang, Y.-T. Long, Z. Ning, Efficient defect-controlled photocatalytic hydrogen generation based on near-infrared Cu-In-Zn-S quantum dots, *Nano Res.* 11 (2018) 1379–1388.
- [33] C. Ye, M.D. Regulacio, S.H. Lim, Q.-H. Xu, M.-Y. Han, Alloyed (ZnS)_x(CuInS₂)_{1-x} semiconductor nanorods: synthesis, bandgap tuning and photocatalytic properties, *Chem. Eur. J.* 18 (2012) 11258–11263.
- [34] X. Yu, X. An, A. Shavel, M. Ibáñez, A. Cabot, The effect of the Ga content on the photocatalytic hydrogen evolution of CuIn_{1-x}Ga_xS₂ nanocrystals, *J. Mater. Chem. A* 2 (2014) 12317–12322.
- [35] S.-C. Zhu, F.-X. Xiao, Transition metal chalcogenides quantum dots: emerging building blocks toward solar-to-hydrogen conversion, *ACS Catal.* 13 (2023) 7269–7309.
- [36] W. Hu, S. Yang, J. Huang, Composition effect on the carrier dynamics and catalytic performance of CuInS₂/ZnS quantum dots for light driven hydrogen generation, *J. Chem. Phys.* 151 (2019), 214705.
- [37] S. Li, S.-M. Jung, W. Chung, J.-W. Seo, H. Kim, S.I. Park, H.C. Lee, J.S. Han, S. B. Ha, I.Y. Kim, S.-I. In, J.-Y. Kim, J. Yang, Defect engineering of ternary Cu-In-Se quantum dots for boosting photoelectrochemical hydrogen generation, *Carbon Energy* (2023), <https://doi.org/10.1002/cey2.384>.
- [38] N. Ali, T.T. Tsega, Y. Cao, S. Abbas, W. Li, A. Iqbal, H. Fazal, Z. Xin, J. Zai, X. Qian, Copper vacancy activated plasmonic Cu_{3-x}SnS₄ for highly efficient photocatalytic hydrogen generation: broad solar absorption, efficient charge separation and decreased HER overpotential, *Nano Res.* 14 (2021) 3358–3364.
- [39] F.A. Kröger, H.J. Vink, Relations between the concentrations of imperfections in crystalline solids, *Solid State Phys.* 3 (1956) 307–435.
- [40] M. Tsuji, S. Iimura, J. Kim, H. Hosono, Hole concentration reduction in CuI by Zn substitution and its mechanism: toward device applications, *ACS Appl. Mater. Interfaces* 14 (2022) 33463–33471.
- [41] J. Du, R. Singh, I. Fedin, A.S. Fuhr, V.I. Klimov, Spectroscopic insights into high defect tolerance of Zn:CuInSe₂ quantum-dot-sensitized solar cells, *Nat. Energy* 5 (2020) 409–417.
- [42] H. Zhao, W. Wang, X. Li, P. Li, M. Cai, Y. You, R. Wang, A.I. Channa, X. Tong, Z. M. Wang, Engineering the interfacial structure of heavy metal-free colloidal heterostructured quantum dots for high-efficiency photoelectrochemical water oxidation without Co-catalyst, *Adv. Energy Sustain. Res.* 4 (2022) 2200142.
- [43] W. Zhang, X. Zhong, Facile synthesis of ZnS–CuInS₂-alloyed nanocrystals for a color-tunable fluorochrome and photocatalyst, *Inorg. Chem.* 50 (2011) 4065–4072.
- [44] G. Kresse, J. Furthmüller, Efficient iterative schemes for ab initio total-energy calculations using a plane-wave basis set, *Phys. Rev. B* 54 (1996) 11169.
- [45] J.P. Perdew, K. Burke, M. Ernzerhof, Generalized gradient approximation made simple, *Phys. Rev. Lett.* 77 (1996) 3865.
- [46] B. Hammer, L.B. Hansen, J.K. Norskov, Improved adsorption energetics within density-functional theory using revised Perdew-Burke-Ernzerhof functionals, *Phys. Rev. B* 59 (1999) 7413.
- [47] S. Grimme, Semiempirical GGA-type density functional constructed with a long-range dispersion correction, *J. Comput. Chem.* 27 (2006) 1787–1799.
- [48] E. Skulason, V. Tripkovic, M.E. Björketun, S. Gudmundsdóttir, G. Karlberg, J. Rossmeisl, T. Bligaard, H. Jonsson, J.K. Norskov, Modeling the electrochemical hydrogen oxidation and evolution reactions on the basis of Density Functional Theory calculations, *J. Phys. Chem. C* 114 (2010) 18182–18197.
- [49] G. Gao, A.P. O'Mullane, A. Du, 2D MXenes: a new family of promising catalysts for the hydrogen evolution reaction, *ACS Catal.* 7 (2017) 494–500.
- [50] B. Yang, X. Mao, F. Hong, W. Meng, Y. Tang, X. Xia, S. Yang, W. Deng, K. Han, Lead-free direct band gap double-perovskite nanocrystals with bright dual-color emission, *J. Am. Chem. Soc.* 140 (2018) 17001–17006.
- [51] J. Yin, P. Maity, R. Naphade, B. Cheng, J.H. He, O.M. Bakr, J.L. Bredas, O. F. Mohammed, Tuning hot carrier cooling dynamics by dielectric confinement in two-dimensional hybrid perovskite crystals, *ACS Nano* 13 (2019) 12621–12629.
- [52] A.L. Efros, V.A. Kharchenko, M. Rosen, Breaking the phonon bottleneck in nanometer quantum dots: role of Auger-like processes, *Solid State Commun.* 93 (1995) 281–284.
- [53] A.L. Efros, M. Rosen, The electronic structure of semiconductor nanocrystals, *Annu. Rev. Mater. Sci.* 30 (2000) 475–521.
- [54] E. Hendry, M. Koeberg, F. Wang, H. Zhang, C. de Mello Donegá, D. Vanmaekelbergh, M. Bonn, Direct observation of electron-to-hole energy transfer in CdSe quantum dots, *Phys. Rev. Lett.* 96 (2006), 057408.
- [55] V.I. Klimov, D.W. McBranch, Femtosecond 1P-to-1S electron relaxation in strongly confined semiconductor nanocrystals, *Phys. Rev. Lett.* 80 (1998) 4028–4031.
- [56] N. Wang, S. Cheong, D.E. Yoon, P. Lu, H. Lee, Y.K. Lee, Y.S. Park, D.C. Lee, Efficient, selective CO₂ photoreduction enabled by facet-resolved redox-active sites on colloidal CdS nanosheets, *J. Am. Chem. Soc.* 144 (2022) 16974–16983.
- [57] Y. Wang, P. Han, X. Lv, L. Zhang, G. Zheng, Defect and interface engineering for aqueous electrocatalytic CO₂ reduction, *Joule* 2 (2018) 2551–2582.
- [58] Y. Sun, Z. Xue, Q. Liu, Y. Jia, Y. Li, K. Liu, Y. Lin, M. Liu, G. Li, C.Y. Su, Modulating electronic structure of metal-organic frameworks by introducing atomically dispersed Ru for efficient hydrogen evolution, *Nat. Commun.* 12 (2021) 1369.
- [59] J. Yang, Y. Shen, Y. Sun, J. Xian, Y. Long, G. Li, Ir nanoparticles anchored on metal-organic frameworks for efficient overall water splitting under pH-universal conditions, *Angew. Chem., Int. Ed.* 62 (2023), 202302220.
- [60] Y. Jia, Z. Xue, J. Yang, Q. Liu, J. Xian, Y. Zhong, Y. Sun, X. Zhang, Q. Liu, D. Yao, G. Li, Tailoring the electronic structure of an atomically dispersed Zinc electrocatalyst: coordination environment regulation for high selectivity oxygen reduction, *Angew. Chem. Int. Ed.* 61 (2022) 202110838.
- [61] S. Li, H. Duan, J. Yu, C. Qiu, R. Yu, Y. Chen, Y. Fang, X. Cai, S. Yang, Cu vacancy induced product switching from formate to CO for CO₂ reduction on copper sulfide, *ACS Catal.* 12 (2022) 9074–9082.
- [62] J. Lin, Y. Shang, X. Li, J. Yu, X. Wang, L. Guo, Ultrasensitive SERS detection by defect engineering on single Cu₂O superstructure particle, *Adv. Mater.* 29 (2017), 1604797.
- [63] C. Peng, G. Luo, J. Zhang, M. Chen, Z. Wang, T.K. Sham, L. Zhang, Y. Li, G. Zheng, Double sulfur vacancies by lithium tuning enhance CO₂ electroreduction to n-propanol, *Nat. Commun.* 12 (2021) 1580.
- [64] Z. Wang, L. Zhang, T.U. Schull, Y. Bai, S.A. Monny, A. Du, L. Wang, Identifying copper vacancies and their role in the CuO based photocathode for water splitting, *Angew. Chem., Int. Ed.* 58 (2019) 17604–17609.
- [65] N. Guo, H. Xue, A. Bao, Z. Wang, J. Sun, T. Song, X. Ge, W. Zhang, K. Huang, F. He, Q. Wang, Achieving superior electrocatalytic performance by surface copper vacancy defects during electrochemical etching process, *Angew. Chem. Int. Ed.* 59 (2020) 13778–13784.
- [66] G. Liu, F. Zheng, J. Li, G. Zeng, Y. Ye, D.M. Larson, J. Yano, E.J. Crumlin, J. W. Ager, L.-w. Wang, F.M. Toma, Investigation and mitigation of degradation mechanisms in Cu₂O photoelectrodes for CO₂ reduction to ethylene, *Nat. Energy* 6 (2021) 1124–1132.
- [67] B. Koo, R.N. Patel, B.A. Korgel, Synthesis of CuInS₂ nanocrystals with trigonal pyramidal shape, *J. Am. Chem. Soc.* 131 (2009) 3134–3135.
- [68] W. Zhu, L. Zhang, P. Yang, C. Hu, H. Dong, Z.-J. Zhao, R. Mu, J. Gong, Formation of enriched vacancies for enhanced CO₂ electrocatalytic reduction over AuCu alloys, *ACS Energy Lett.* 3 (2018) 2144–2149.
- [69] A. Shabaev, M.J. Mehl, A.L. Efros, Energy band structure of CuInS₂ and optical spectra of CuInS₂ nanocrystals, *Phys. Rev. B* 92 (2015), 035431.
- [70] W. van der Stam, M. de Graaf, S. Gudjonsson, J.J. Geuchies, J.J. Dijkema, N. Kirkwood, W.H. Evers, A. Longo, A.J. Houtepen, Tuning and probing the distribution of Cu⁺ and Cu²⁺ trap states responsible for broad-band photoluminescence in CuInS₂ nanocrystals, *ACS Nano* 12 (2018) 11244–11253.
- [71] T. Ding, G. Liang, J. Wang, K. Wu, Carrier-doping as a tool to probe the electronic structure and multi-carrier recombination dynamics in heterostructured colloidal nanocrystals, *Chem. Sci.* 9 (2018) 7253–7260.
- [72] Y. Li, R. Lai, X. Luo, X. Liu, T. Ding, X. Lu, K. Wu, On the absence of a phonon bottleneck in strongly confined CsPbBr₃ perovskite nanocrystals, *Chem. Sci.* 10 (2019) 5983–5989.
- [73] S. Wang, J. Leng, Y. Yin, J. Liu, K. Wu, S. Jin, Ultrafast dopant-induced exciton Auger-like recombination in Mn-doped perovskite nanocrystals, *ACS Energy Lett.* 5 (2020) 328–334.
- [74] K. Zheng, K. Židek, M. Abdellah, W. Zhang, P. Chábbera, N. Lenngren, A. Yartsev, T. Pullerits, Ultrafast charge transfer from CdSe quantum dots to p-Type NiO: Hole injection vs hole trapping, *J. Phys. Chem. C* 118 (2014) 18462–18471.
- [75] S. Logunov, T. Green, S. Marguet, M.A. El-Sayed, Interfacial carriers dynamics of CdS nanoparticles, *J. Phys. Chem. A* 102 (1998) 5652–5658.
- [76] V.I. Klimov, D.W. McBranch, C.A. Leatherdale, M.G. Bawendi, Electron and hole relaxation pathways in semiconductor quantum dots, *Phys. Rev. B* 60 (1999) 13740–13749.
- [77] B.R.C. Vale, E. Socie, A. Burgos-Caminal, J. Bettini, M.A. Schiavon, J.E. Moser, Exciton, biexciton, and hot exciton dynamics in CsPbBr₃ colloidal nanoplatelets, *J. Phys. Chem. Lett.* 11 (2020) 387–394.

- [78] L. Cheng, X. Yue, J. Fan, Q. Xiang, Site-specific electron-driving observations of CO₂-to-CH₄ photoreduction on Co-doped CeO₂/crystalline carbon nitride S-scheme heterojunctions, *Adv. Mater.* 34 (2022), 2200929.
- [79] X. Chen, C. Peng, W. Dan, L. Yu, Y. Wu, H. Fei, Bromo- and iodo-bridged building units in metal-organic frameworks for enhanced carrier transport and CO₂ photoreduction by water vapor, *Nat. Commun.* 13 (2022) 4592.
- [80] X. Shi, C. Dai, X. Wang, J. Hu, J. Zhang, L. Zheng, L. Mao, H. Zheng, M. Zhu, Protruding Pt single-sites on hexagonal ZnIn₂S₄ to accelerate photocatalytic hydrogen evolution, *Nat. Commun.* 13 (2022) 1287.
- [81] M. Cai, Q. Liu, Z. Xue, Y. Li, Y. Fan, A. Huang, M.-R. Li, M. Croft, T.A. Tyson, Z. Ke, G. Li, Constructing 2D MOFs from 2D LDHs: a highly efficient and durable electrocatalyst for water oxidation, *J. Mater. Chem. A* 8 (2020) 190–195.
- [82] M. Cai, Q. Liu, Y. Zhao, Z. Wang, Y. Li, G. Li, Accelerating charge transfer at an ultrafine NiFe-LDHs/CB interface during the electrocatalyst activation process for water oxidation, *Dalton Trans.* 49 (2020) 7436–7443.
- [83] A. Liu, H. Zhu, W.-T. Park, S.-J. Kim, H. Kim, M.-G. Kim, Y.-Y. Noh, High-performance p-channel transistors with transparent Zn doped-CuI, *Nat. Commun.* 11 (2020) 4309.
- [84] X. Yan, M. Xia, H. Liu, B. Zhang, C. Chang, L. Wang, G. Yang, An electron-hole rich dual-site nickel catalyst for efficient photocatalytic overall water splitting, *Nat. Commun.* 14 (2023) 1741.
- [85] H. Sheng, J. Wang, J. Huang, Z. Li, G. Ren, L. Zhang, L. Yu, M. Zhao, X. Li, G. Li, N. Wang, C. Shen, G. Lu, Strong synergy between gold nanoparticles and cobalt porphyrin induces highly efficient photocatalytic hydrogen evolution, *Nat. Commun.* 14 (2023) 1528.
- [86] Q. Mo, L. Zhang, S. Li, H. Song, Y. Fan, C.Y. Su, Engineering single-atom sites into pore-confined nanospaces of porphyrinic metal-organic frameworks for the highly efficient photocatalytic hydrogen evolution reaction, *J. Am. Chem. Soc.* 144 (2022) 22747–22758.
- [87] W. Yang, R.R. Prabhakar, J. Tan, S.D. Tilley, J. Moon, Strategies for enhancing the photocurrent, photovoltage, and stability of photoelectrodes for photoelectrochemical water splitting, *Chem. Soc. Rev.* 48 (2019) 4979–5015.
- [88] W. Yang, Q. Liu, J. Yang, J. Xian, Y. Li, G. Li, C.-Y. Su, Ultrafine PdRu nanoparticles immobilized in metal-organic frameworks for efficient fluorophenol hydrodefluorination under mild aqueous conditions, *CCS Chem.* 4 (2022) 2276–2285.
- [89] Z. Fang, B. Bueken, D.E. DeVos, R.A. Fischer, Defect-engineered metal-organic frameworks, *Angew. Chem. Int. Ed.* 54 (2015) 7234–7254.
- [90] L. Dai, A. Dong, X. Meng, H. Liu, Y. Li, P. Li, B. Wang, Enhancement of visible-light-driven hydrogen evolution activity of 2D pi-conjugated bipyridine-based covalent organic frameworks via post-protonation, *Angew. Chem. Int. Ed.* 62 (2023), 202300224.
- [91] P. Da, Y. Zheng, Y. Hu, Z. Wu, H. Zhao, Y. Wei, L. Guo, J. Wang, Y. Wei, S. Xi, C. H. Yan, P. Xi, Synthesis of bandgap-tunable transition metal sulfides through gas-phase cation exchange-induced topological transformation, *Angew. Chem. Int. Ed.* 135 (2023), 202301802.
- [92] C. Cheng, J. Zhang, B. Zhu, G. Liang, L. Zhang, J. Yu, Verifying the charge-transfer mechanism in S-scheme heterojunctions using femtosecond transient absorption spectroscopy, *Angew. Chem. Int. Ed.* 62 (2023), 202218688.
- [93] S. Yu, X.B. Fan, X. Wang, J. Li, Q. Zhang, A. Xia, S. Wei, L.Z. Wu, Y. Zhou, G. R. Patzke, Efficient photocatalytic hydrogen evolution with ligand engineered all-inorganic InP and InP/ZnS colloidal quantum dots, *Nat. Commun.* 9 (2018) 4009.
- [94] Y. Liu, C.H. Liu, T. Debnath, Y. Wang, D. Pohl, L.V. Besteiro, D.M. Meira, S. Huang, F. Yang, B. Rellinghaus, M. Chaker, D.F. Perepichka, D. Ma, Silver nanoparticle enhanced metal-organic matrix with interface-engineering for efficient photocatalytic hydrogen evolution, *Nat. Commun.* 14 (2023) 541.
- [95] J. Kosco, S. Gonzalez-Carrero, C.T. Howells, T. Fei, Y. Dong, R. Sougrat, G. T. Harrison, Y. Firdaus, R. Sheelamantula, B. Purushothaman, F. Moruzzi, W. Xu, L. Zhao, A. Basu, S. De Wolf, T.D. Anthopoulos, J.R. Durrant, I. McCulloch, Generation of long-lived charges in organic semiconductor heterojunction nanoparticles for efficient photocatalytic hydrogen evolution, *Nat. Energy* 7 (2022) 340–351.
- [96] Z. Li, T. Deng, S. Ma, Z. Zhang, G. Wu, J. Wang, Q. Li, H. Xia, S.W. Yang, X. Liu, Three-component donor-pi-acceptor covalent-organic frameworks for boosting photocatalytic hydrogen evolution, *J. Am. Chem. Soc.* 145 (2023) 8364–8374.
- [97] W. Dong, Z. Qin, K. Wang, Y. Xiao, X. Liu, S. Ren, L. Li, Isomeric oligo (phenylenevinylene)-based covalent organic frameworks with different orientation of imine bonds and distinct photocatalytic activities, *Angew. Chem., Int. Ed.* 62 (2023) 202216073.
- [98] H. Su, W. Wang, R. Shi, H. Tang, L. Sun, L. Wang, Q. Liu, T. Zhang, Recent advances in quantum dot catalysts for hydrogen evolution: synthesis, characterization, and photocatalytic application, *Carbon Energy* 5 (2023), e280.
- [99] Z. Li, A.I. Channa, Z.M. Wang, X. Tong, Tailoring eco-friendly colloidal quantum dots for photoelectrochemical hydrogen generation, *Small* (2023), <https://doi.org/10.1002/smll.202305146>.
- [100] M. Cai, X. Tong, P. Liao, S. Shen, H. Zhao, X. Li, L. Xia, H. Zhi, N. Zhou, Z. Xue, L. Jin, J. Li, G. Li, F. Dong, A.V. Kabashin, Z.M. Wang, Manipulating the optically active defect-defect interaction of colloidal quantum dots for carbon dioxide photoreduction, *ACS Catal.* (2023), <https://doi.org/10.1021/acscatal.3c03884>.